

# Boundary Erosion by Granular Flows in Centrifuge Experiments: Preliminary Results

Chi-Yao HUNG,<sup>1,2,\*</sup> Hervé CAPART<sup>1</sup>, Colin P. STARK<sup>2</sup>, and Liming LI<sup>3</sup>

<sup>1</sup> Dept. of Civil Engineering & Hydrotech Research, National Taiwan University, Taipei, Taiwan

<sup>2</sup> Lamont-Doherty Earth Observatory, Columbia University, New York, NY, USA

<sup>3</sup> Dept. of Civil Engineering and Engineering Mechanics, Columbia University, New York, NY, USA

\*Corresponding author. E-mail: d00521008@ntu.edu.tw

Boundary forces generated by debris flows can be powerful enough to erode bedrock and cause considerable damage to infrastructure during runout. Performing experiments large enough to generate realistic boundary forces is a challenge. An alternative is to run table-top simulations with unnaturally weak but fast-eroding pseudo-bedrock, another is to extrapolate from micro-erosion of natural substrates driven by unnaturally weak impacts. Here we take a different approach in which we scale up the granular impact forces by running experiments under enhanced gravity in a geotechnical centrifuge. We deploy a 40cm-diameter rotating drum on the centrifuge at effective gravity levels up to 100 g, and generate analog debris flows with an effective flow depth of over several meters. We study the boundary erosion effects of these dense granular flows (1) by using high speed video and particle tracking to measure their velocity fields, and (2) by mapping patterns of wear in a synthetic bedrock wall plate using 3d microphotogrammetric methods. By combining these experimental results with theoretical developments, we have the ingredients we need for constructing an erosion law for sliding wear at the margins of a dense granular flow.

**Key words:** debris flow, bedrock erosion, natural hazards, centrifuge experiments

## 1. INTRODUCTION

When flowing through bedrock canyons or past reinforced concrete structures, debris flows can abrade and damage lateral and bottom boundaries. Such damage processes are difficult to study in-situ during events, both because their timing and location is difficult to anticipate and because such flows can easily destroy instrumentation. Knowledge gained from the field is therefore mostly limited to observations acquired after events and is often qualitative in nature.

As an example, we have carried out field studies on the debris flow impacts of Typhoon Morakot, which made landfall on Taiwan on 7-9 August 2009. This tropical cyclone brought 24 hour rainfall accumulations exceeding 500 mm to mountainous terrain in the south-west of the island, and 3000 mm total accumulations were recorded at several gauges [Chien and Kuo, 2011; Xie and Zhang, 2012]. Heavy mass-wasting ensued, such as along the Putunpunas River, a tributary of the Laonong River (Fig. 1), which suffered massive landsliding and subsequent debris flow. Sediment from this and nearby tributary

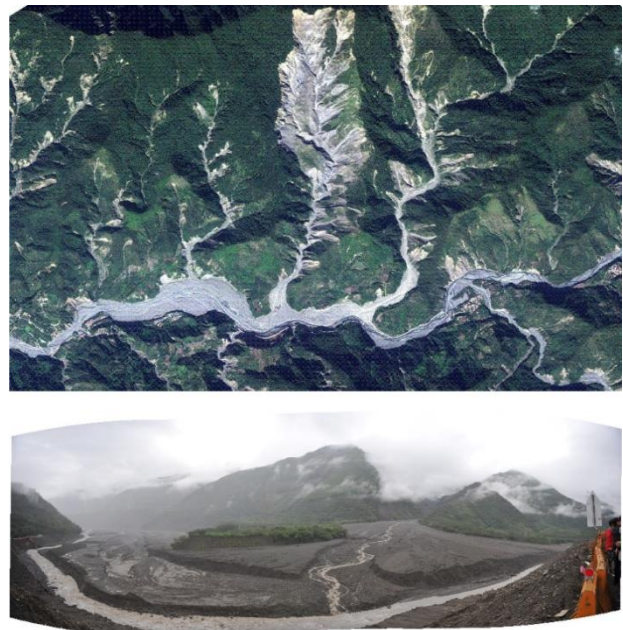


**Fig. 1** Typhoon Morakot landslides and debris flows and after-effects: Putunpunas, SW Taiwan.

flows has raised the bed-level of the Laonong River by about 30 m. The feeder canyon for the Putunpunas debris flow is shown in **Fig. 2**: its shape is the result of boundary erosion by multiple, similarly powerful debris flows over millennia.



**Fig. 2** Debris-flow channel, Putunpunas River, Taiwan

In this paper, we demonstrate the feasibility of running laboratory experiments on analog debris flows that simulate this kind of wear process in a controlled environment. Our goal is to use data from such experiments to develop a semi-empirical boundary erosion law for debris flows.

## 2. EXPERIMENTAL DESIGN

In their review of empirical data on dense granular flow, *GDR Midi* [2004] summarize the wide range of apparatus used in such experiments (see also *Takashi*, [1991] and *Forterre and Pouliquen*, [2008]). Of particular interest here are heap and drum flow apparatus. Heap flow rigs are popular in debris flow experiments [e.g., *Savage*, 1984; *Ahn et al.*, 1991; *Major*, 1997; *Iverson*, 1997; *Azanza et al.*, 1999; *Parsons et al.*, 2001]. Typically single event, short duration flows are generated, making any study of their long-term erosive effects impractical. In contrast, drum-driven flows are less realistic, but they provide a form of recirculating flume that makes long-term erosion study feasible. The work of *Hsu*, [2010] is a good example: she used a 4 m-diameter drum to drive thin, persistent flows using a range of media mixtures (sand, gravel, mud, water) [*Hsu et al.*, 2010]. Drum-driven granular flows have wide industrial application, and there is a substantial literature on their use [*Ristow*, 1996; *Buchholtz and Pöschel*, 1997; *Boateng*, 1998; *Ding et al.*, 2001]. Their mechanics have been widely studied if not fully understood.

We opted to use a small (0.4 m-diameter) drum to study the effects of erosive granular flows. Unlike the *Hsu*, [2010] experiments that studied thin flows by loading the drum with a small amount of sediment, we used a half-filled drum to drive a central zone of

channelized granular avalanching. Instead of studying wear caused by impacts at the frontal tongue of a simulated debris flow [*Hsu et al.*, 2008], we looked at the wear induced by frictional sliding along the drum wall. Despite its relevance to debris-flow driven erosion, this sliding wear process has not been widely studied.

### 2.1 Scaling-up granular flows

A key goal was to study the erosion of materials with strength and erodibility properties similar to real rocks. To achieve this we needed to work with granular flows whose boundary forces match those of natural debris flows. Rather than building a very large drum [e.g., *Hsu*, 2010] and working with large grain impacts, we scaled up small-grain impact forces by running our drum experiments under enhanced gravity in a geotechnical centrifuge (**Fig. 3**). *Brucks et al.*, [2007] were the first to demonstrate the feasibility of performing drum-based granular flow experiments on a geotechnical centrifuge. Partly inspired by their work, we built a similar drum apparatus (**Fig. 4**) for deployment on the 100-g-ton centrifuge in the Carleton Laboratory at Columbia University (**Fig. 3**).



**Fig. 3** Geotechnical centrifuge in the Carleton Laboratory at Columbia University, with drum mounted on payload bay.

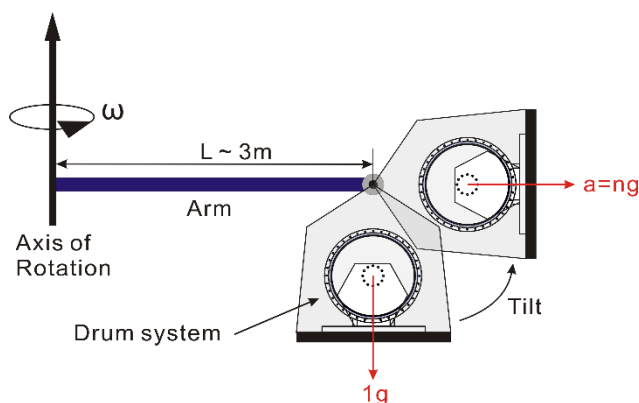


**Fig. 4** Schematic of centrifuge and drum deployment

## 2.2 Semi-analytical model of dense, shallow granular flow over a loose bed

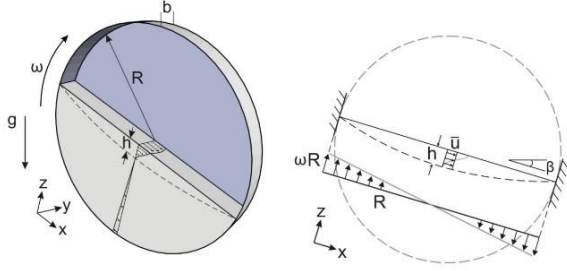


**Fig. 5** Left: drum of radius  $R$  and effective width  $b$  rotates at angular velocity  $\omega$ , driving grain flow of max depth  $h$ . Right: flow layer at angle  $\beta$  and mean velocity  $\bar{u}$ . Rotation imposes a basal mass input/output of  $\pm \omega R^2/2$ .

To help guide experimental design and choice of design parameters, we formulated a simple theory of grain flow in a half-filled rotating drum (**Fig. 5**). Drum rotation at a constant angular velocity  $\omega$  drives grain avalanching at an angle  $\beta$  with a flow depth  $h$ . We simplify the flow geometry by mapping the rotation into a simple shear normal to the  $x$  axis that feeds mass input/output at the flow bottom boundary (**Fig. 5 right**). The discharge in the flow layer at the rotation axis ( $x=0$ ) is

$$q = \frac{\omega R^2}{2} \quad (1)$$

which is also the maximum discharge. After mapping into simple shear, this discharge stays the same (1) and indicates the maximum  $z$ -component of the velocity can be written as  $w = \omega x$ . At the rotation axis ( $x=0$ ), the discharge can be written as the product of the average velocity  $\bar{u}$  and the flow depth  $h$  i.e.,  $q = h\bar{u}$ . Combining these equations gives the ratio of mean horizontal velocity to maximum vertical velocity as

$$\frac{\bar{u}}{w} = \frac{R}{2h} \quad (2)$$

When  $R \gg h$  it follows that  $\bar{u} \gg w$  i.e., the  $z$ -component of the velocity is much smaller than the  $x$ -component. We can therefore apply the shallow water approximation.

We consider a shallow layer of homogenous dry granular material flowing over a bed inclined at an angle  $\beta$  composed of identical granular material. The channel width is defined as  $b$  and the 2D governing equations can be written as

$$\left\{ \begin{array}{l} \frac{\partial u}{\partial x} + \frac{\partial w}{\partial z} = 0 \\ \frac{\partial u}{\partial t} + u \frac{\partial u}{\partial x} + w \frac{\partial u}{\partial z} + \frac{1}{\rho} \frac{\partial \sigma}{\partial x} = g \sin \beta + \frac{1}{\rho} \frac{\partial \tau}{\partial z} - \frac{2\tau_{\pm}}{\rho b} \\ \frac{1}{\rho} \frac{\partial \sigma}{\partial z} = -g \cos \beta \end{array} \right. \quad (3)$$

The symbols  $\tau$  and  $\tau_{\pm}$  correspond to the shear stresses acting on the deposit and the wall, and  $\sigma$  is the total normal stress. By assuming steady uniform flow, the derivative terms in (3) in  $x$  and  $t$  vanish. Defining a depth coordinate parameter  $\eta$  measured from the free surface, the governing equations (3) simplify to

$$\left\{ \begin{array}{l} \frac{\partial \tau}{\partial \eta} = \rho g \sin \beta - \frac{2\tau_{\pm}}{b} \\ \frac{\partial \sigma}{\partial \eta} = \rho g \cos \beta \end{array} \right. \quad (4)$$

The total normal stress  $\sigma$  is found by integrating the second equation in (4) using the boundary condition at the free surface, i.e.,  $\sigma = 0$  at  $\eta = 0$ , to give

$$\sigma = \rho g \eta \cos \beta \quad (5)$$

Now we introduce a constitutive model for the shear stress. We adopt the linearized dense granular flow rheology [*GDR MiDi*, 2004; *da Cruz et al.*, 2005; *Berzi and Jenkins*, 2009]

$$\tau = (\tan \alpha + \chi I) \sigma \quad (6a)$$

$$I = \frac{\dot{\gamma} D}{\sqrt{\sigma/\rho}} \quad (6b)$$

where  $\alpha$  is the internal angle of friction in the limit of large deformation and very slow deformation rate, and  $\chi$  is a dimensionless constant. The inertial number  $I$  normalizes the product of deformation rate  $\dot{\gamma} = \partial u / \partial z$  and grain diameter  $D$ . The shear stress on the wall can be approximated as [*Jop et al.*, 2005]

$$\tau_{\pm} = \mu_{\pm} \sigma \quad (7)$$

Substituting the shear stress and normal stress into the governing equation (3), integrating over the flow depth, and applying the boundary conditions at the free surface and at the bottom, gives the velocity profile

$$u(\eta) = \frac{\mu_{\pm}}{b} \frac{\sqrt{g \cos \beta}}{\chi D} \left\{ \frac{2}{3} h (h^{3/2} - \eta^{3/2}) - \frac{2}{5} (h^{5/2} - \eta^{5/2}) \right\} \quad (8)$$

where  $h = b(\tan \beta - \tan \alpha) / \mu_{\pm}$ . Integrating this velocity profile from 0 to  $h$  yields the depth-averaged velocity

$$\bar{u} = \frac{1}{h} \int_0^h u(\eta) d\eta = \frac{\mu_{\pm}}{b} \frac{\sqrt{g \cos \beta}}{\chi D} \frac{4}{35} h^{5/2} \quad (9)$$

Substituting this depth-averaged velocity into the definition of maximum discharge, we obtain

$$q = h\bar{u} = \frac{4}{35} \mu_{\pm} \frac{\sqrt{g \cos \beta}}{\chi D b} h^{7/2} \quad (10)$$

When carrying out dimensionless analysis of this problem, we can use the fact that the model discharge in (10) is equal to the drum discharge defined in (1), to obtain the following. From the relationship between the drum rotation rate and the dynamic angle of repose, we can define a kind of Froude number

$$\begin{aligned} Fr &= \frac{\omega^2 R}{g} \\ &= \frac{(8/35)^2}{\chi^2 \mu_{\pm}^5} \left(\frac{D}{R}\right)^3 \left(\frac{W}{D}\right)^5 (\tan \beta - \tan \alpha)^7 \cos \beta \end{aligned} \quad (11)$$

This dimensionless number reveals an important property: if we simultaneously fix both the ratio of grain diameter to drum radius, and the ratio of drum width to grain diameter, we maintain the same granular flow regime – a result deduced empirically by *Brucks et al.*, [2007]. This is because, as inspection of (11) reveals, in so doing we maintain a balance between effective gravity and rotation rate. We use this result below to help choose design parameters.

### 2.3 Technical constraints

Channelized granular flows only a few grains wide exhibit a finite grain-number effect that complicates application of a simple frictional rheology. To avoid this phenomenon, we require the channel width to be at least ten times the grain diameter. To impose a long width-length aspect ratio on the flow, we set the diameter of the drum at over ten times the channel width.

Running experiments on a 100-g-ton geotechnical centrifuge imposes several limits on the experimental setup. Particularly important limits are set by: (1) the power supply to the centrifuge payload, and (2) technical limitations of the video camera.

First, the power supply. The major power drain on the centrifuge payload is the drum motor when run at high effective  $g$ . We can estimate the torque for the most power-demanding scenario, in which all the grains in the half-filled drum spin at the same rate as the drum. A rough estimate gives a torque of

$$T = \rho_{bulk} g_{level} g \frac{\pi R^2}{2} b \frac{R}{2} \quad (12)$$

The power requirement is the product of the torque and the rotation rate. Since the rotation rate is related to  $Fr$ , we can rewrite the relationship as

$$P_{max} = T\omega = \rho_{bulk} g_{level} \frac{3}{2} g \frac{\pi R^2}{2} b \frac{R}{2} \sqrt{\frac{Fr g}{R}} \quad (13)$$

We can rearrange this equation to give a relationship between  $Fr$  and effective  $g$  for a given power supply limit  $P_{max}$

$$Fr = \frac{\left[ (\rho_{bulk} g \frac{\pi R^2}{2} b \frac{R}{2} \sqrt{\frac{g}{R}})^{-1} P_{max} \right]^2}{g_{level}^3} \quad (14)$$

Second, the video camera. Using Froude-number scaling as a guide, we can predict that to maintain the same flow regime from low to high effective  $g$ , an increasing rotation rate will be needed, and as a result, grains will move much faster. In order to capture the grain motion accurately from one video frame to the next, grain displacement must be less than 1 grain diameter per frame ( $\Delta t < D/2\bar{u}$ ). Using  $q = h\bar{u}$ , (1), and (11), the Froude number as a function of minimum camera frame rate (frames-per-second or FPS) is estimated at

$$Fr \leq \left( \frac{hD}{\sqrt{g} R^{3/2}} \times FPS \right)^2 \quad (15)$$

Equations (14) and (15) predict the parameter space accessible to centrifuge experiments. Their behavior for our ultimate choice of design parameters is illustrated in **Fig. 6**.

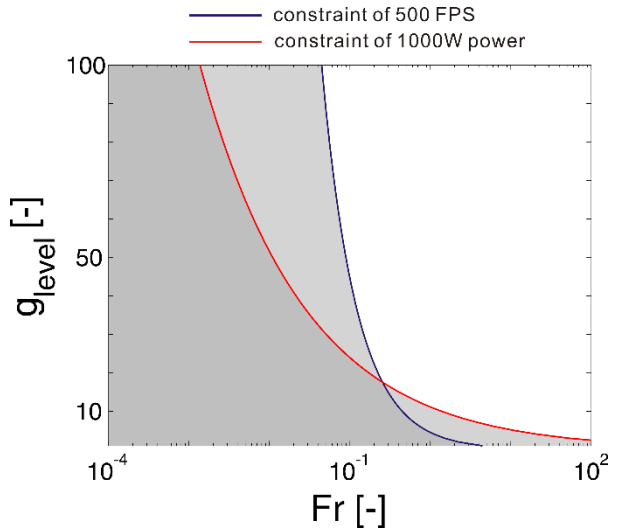


**Fig. 6** Parameter space accessible to experimentation predicted by (14) and (15).

## 2.4 Choice of design parameters

Our primary design goal is to drive steady granular avalanching on the drum such that we mimic debris flow erosion at drum wall. As *Brucks et al.*, [2007] have shown, the flow regime on a drum is roughly predicted by  $Fr$  and effective  $g$ , so we can use (14) and (15) to identify suitable design parameters. Our main constraint is a maximum power available on the centrifuge payload of  $P_{max} = 1$  kW. Taking into consideration the physical space available ( $\sim 1$ m) on the payload, the maximum  $g$  level (100g), material densities, and a reasonable grain size range of  $D=2.3\text{--}4$  mm, we settled on a drum of radius  $R=200$  mm (**Fig. 7**) built of aluminum.

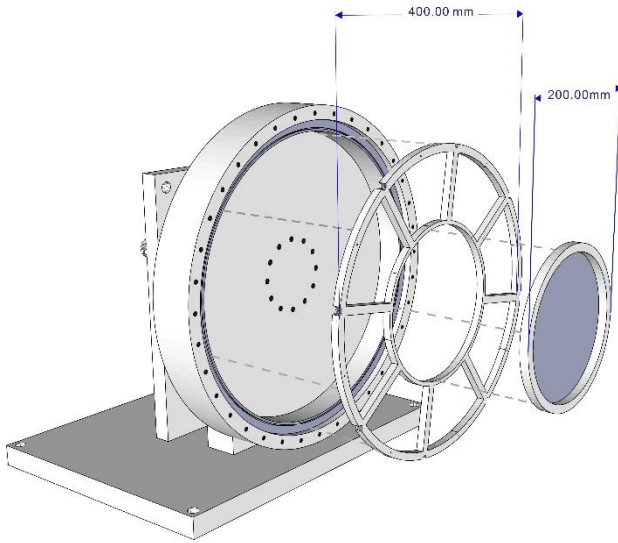


**Fig. 7** Placement of the 200mm-diameter erosion plate within the drum using a 400mm wheel-like frame.

## 2.5 Erosion plate properties

To simulate debris-flow-driven boundary erosion, we embed a disk of synthetic rock into the wall of the drum (**Fig. 7**). Grain flow past this erosion plate drives sliding wear at rates determined by the strength of the rock, grain size, speed and depth of flow, and effective  $g$  on the centrifuge. We chose to mount the synthetic rock on an aluminum plate with radius 100 mm and depth 10 mm.

For the synthetic rock, we chose a mixture of gypsum, sand and water. After some experimentation with different mixture proportions, we settled on a gypsum:sand of ratio 70:30. Similar to the process of making a concrete sample, the mixture needs time to reach maximum strength. We ran a series of strength tests over time, measuring both compressive and tensile strength (**Fig. 8**). Although a stable, limit strength was not found, by comparing compressive strength with density, we deduced that the synthetic rock mixture reaches a limit strength after about 20 days.

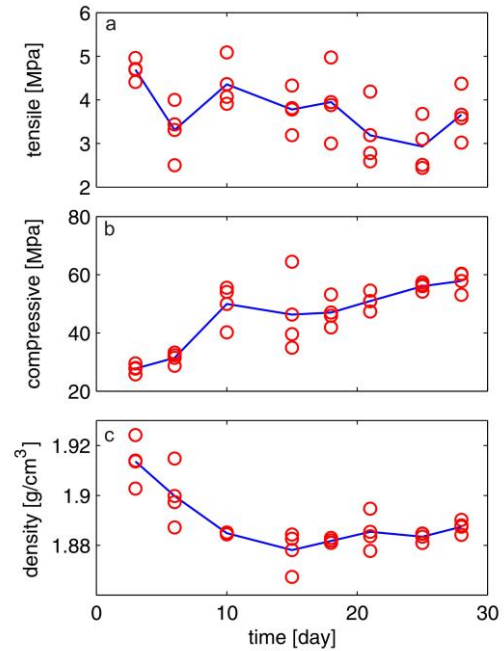


**Fig. 8** Lab measurements of synthetic bedrock properties: (a) tensile test; (b) compression test; (c) density. The blue lines indicate mean values.

## 2.6 High-speed video camera properties

As **Fig. 6** and (15) show, the accessible range of  $Fr$  is potentially limited by the camera for frame rates of around 500fps. To avoid this limitation, we deployed a faster video camera, a Phantom Miro 320s, which delivers a raw image size of 1400x1210 at 1800 fps. By placing the camera orthogonally in front of the drum at a distance of 400 mm, and by using a 16 mm wide-angle C-mount lens, we were able to view the entire drum with little distortion (**Fig. 9**). Image acquisition was controlled remotely over wifi during centrifuge runs, allowing us to record 2-3s bursts of video at a series of effective  $g$ -levels and drum rotation rates during a single run.

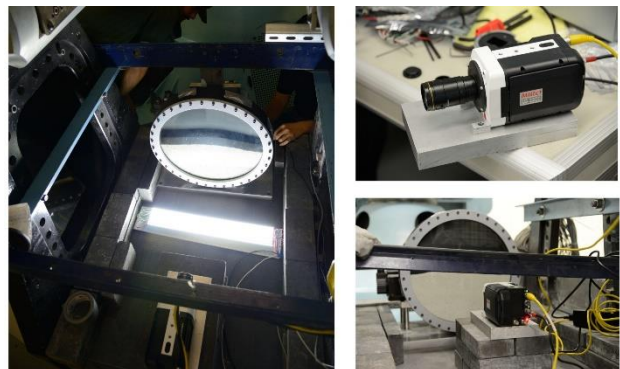


**Fig. 9** Camera deployment on the centrifuge payload.

### 3. IMAGING MEASUREMENTS

#### 3.1 Grain flow velocity field

Particle tracking velocimetry (PTV) has been applied in wide range of experimental contexts [Adrain, 1991] and has been shown to be capable of high accuracy. Our research group has adapted the PTV method and developed code tailored to tracking ensemble coarse grain motions [Capart, 2002; Ni, 2005]. The code was adapted further during the present study to address the particular challenges posed by drum-driven granular avalanching.

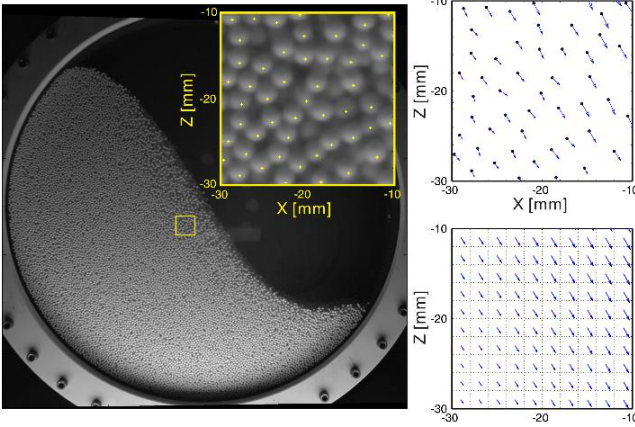


Fig. 10 Particle tracking velocimetry (PTV).<sup>1</sup>

The PTV image processing sequence is illustrated in Fig. 10. First, we use a calibration plate to measure the drum-sensor distance and to establish a mapping between the images and the drum. We then project each image into a Cartesian coordinate system whose origin is at the center of the drum. Next we identify characteristic points on the grains (Fig. 10, left inset, yellow points) using filtering techniques. By pairing grains in successive images based on their proximity, we track apparent grain displacements over time and obtain a time series of grain velocity fields (Fig. 10 top right). Since the drum apparatus generates steady non-uniform flow, we chose to bin and average the grain velocities over multiple frames (here we use 4980 frames lasting 2.77s) to obtain gridded velocity fields (Fig. 10 right bottom) – one for each experiment, with empty cells where no grain velocities were resolved in any of the frame pairs.

Despite the use of time-averaging, there is always a large number of empty grid cells, particularly near the free upper surface where saltating grains are imaged. Since our focus is dense granular flow, we need to process the gridded velocity fields further to eliminate the empty cells and to obtain a smooth free surface boundary. Instead of simply interpolating, a better strategy is to exploit the stream function of the grain flow field as follows. First, we need to accurately identify the rotation center  $(x_c, y_c)$  and rotation rate  $\omega$ , which we can do with the aid of the

grain motions observed outside the avalanching layer. These grains (each at  $(x_i, y_i)$ ) move in rigid body rotation  $(u_i, v_i)$  with the drum, which can be written as

$$\begin{bmatrix} y_i & 0 & -1 \\ x_i & -1 & 0 \end{bmatrix} \begin{bmatrix} \omega \\ \omega x_c \\ \omega y_c \end{bmatrix} = \begin{bmatrix} u_i \\ -v_i \end{bmatrix} \quad (16)$$

We solve this overdetermined system of  $i=1, \dots, N$  (where  $N$ =total number of grid cells) equations using least squares. We then subtract this rigid body rotation field from the velocity mesh.

Next, we obtain the stream function from the velocity mesh on a staggered grid ( $\psi_i$ ), paying special attention to where the grid is cut by the outer (grain-drum) boundary. Within the main flow field, we can write the stream function as

$$\frac{\partial \psi_i}{\partial y} = u_i \quad (17)$$

$$\frac{\partial \psi_i}{\partial x} = -v_i$$

In the region of the outer boundary, we interpolate the stream function  $\psi$  between the resolved staggered grid values and zero at the curved boundary

$$\psi_j = b_0 d_j \quad (18)$$

Where the distances  $d_j$  are measured between the cut grid vertices and the boundary. We combine (17) and (18) and solve for the stream function  $\psi$  using least squares. In this way we obtain a continuous grid of  $\psi$  values with a smooth upper boundary at the granular flow surface. The velocity field  $(u_i', v_i')$  recomputed from this stream function shares this smooth upper boundary, which allows for easier determination of the granular flow layer.

Since the stream function is the flux through a given interval, we can use it to identify a simply continuous region of grain flow. We arbitrarily set a threshold of 1% on the normalized stream function grid, i.e., we identify the flow layer grid cells  $k$  by finding

$$k : \psi_k \geq \frac{\omega R^2 / 2}{100} \quad (19)$$

#### 3.2 Multitemporal mapping of erosion patterns

As Fig. 5 shows, drum rotation drives a lens-shaped zone of granular flow at whose wall boundaries frictional sliding takes place. Our goal is to induce erosion on the synthetic rock plate embedded in the back wall and to measure the pattern and degree of erosion over a series of experiments. To achieve the latter, we developed a novel method of microtopographic mapping based on close-range photography and modern photogrammetric techniques, specifically structure-from-motion and

multiview stereo [Verhoeven, 2011; Fonstad et al., 2013] provided by the commercial software tool PhotoScan created by AgiSoft. We needed to map microtopography at a resolution of  $\sim 1$  mm to a vertical precision of  $\sim 100$   $\mu\text{m}$  over the entire 200 mm-diameter erosion plate. To achieve this level of precision, we used a 36 Mpixel professional DSLR with a good quality, 35 mm prime lens. Sixteen accurately measured ground control points arrayed around the erosion plate guided calibration and scaling, and the lighting was carefully controlled. We were able to construct a 3D topographic model of the required resolution with a set of only 16 oblique photos taken at a distance of 350 mm arranged as shown in **Fig. 11**.

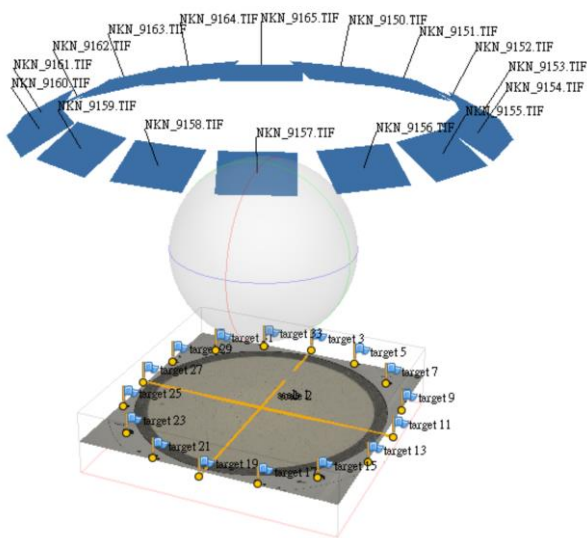


**Fig. 11** Microphotogrammetric mapping of erosion plate

#### 4. PRELIMINARY RESULTS

We ran a series of experiments at different effective  $g$  levels and rotation rates, first to explore the granular flow behavior (**Fig. 12**), and then to study the boundary erosion process (**Table 1**).

As regards the flow behavior, our results are in broad agreement with *Brucks et al.*, [2007] in that we see a series of flow regimes from intermittent avalanching, to continuous planar avalanching, to avalanching with a sigmoidal free (upper) surface, all approximately delimited by Froude number.

**Fig. 12** illustrates these results. The left-hand column shows long-exposure images generated from about 100 video frames spanning a little over 0.05 s. These images demonstrate the broad dependence of flow geometry on Froude number: first, as the rotation rate is increased from low (2 rpm,  $Fr \sim 0.001$ ) to high (20 rpm,  $Fr \sim 0.1$ ; bottom to middle images) and the free upper flow surface ranges from planar to sigmoidally curved; second, as effective gravity is

increased from 1  $g$  to 50  $g$  ( $Fr \sim 0.002$ ) and the free surface is forced to return to a planar form (middle to top images). The middle column visualizes some raw results from PTV mapping of the velocity field: warm colors indicate high granular flow speeds, while cool colors indicate slower flow. Notice the similarity of the flow field patterns at 1  $g$  and 2 rpm (bottom) and at 50  $g$  and 20 rpm (top), i.e., at similar Froude number  $Fr$ , together with their order-of-magnitude difference in granular flow speed. The right column shows the streamlines (pink) derived using (16)–(18) and the base of the granular flow layer estimated using (19) (green). The flow layer is thinner at 1  $g$  and 2 rpm (bottom) and at 50  $g$  and 20 rpm (top), i.e., lower  $Fr$ , and thicker at 1  $g$  and 20 rpm (middle), i.e., at higher  $Fr$ . By combining the granular flow fields with the flow layer boundaries identified using the streamlines, we can make the measurements of grain-wall velocity and stress that will be essential ingredients in an empirical erosion law. The remaining element is to measure bedrock erosion rates driven by these flows.

Exploring this question, **Table 1** summarizes the series of experiments we subsequently carried out with the synthetic rock erosion plate placed axially on the drum wall (**Fig. 7**). The rock surface in its initial state (S1) was smooth and flat, and its microtopography was mapped before and after progressive erosion at various effective  $g$  levels, rotation rates, and grain types (**Figs. 11, 13**). By experimenting with these parameters we identified conditions under which erosion takes place and conditions for which it does not.

We observed negligible erosion at low effective  $g$  (S2 to S3), centrally localized erosion at high  $g$  with spherical (2.3 mm and 4 mm, mean diameter) grains (S1 to S2, S3 to S4, S6 to S7, S7 to S8), and faster erosion over a broader area with angular 4 mm grains (S4 to S5, S5 to S6) (**Figs. 13, 14**). We tentatively find that, by fixing the flow depth while tuning the grain size and rotation rate (S6 to S7 and S7 to S8), faster flow speeds and larger grain sizes strongly enhance erosion. It is important to remember that these patterns of plate erosion are the result of angular integration (as the drum rotates) of a spatially variable wear rate field induced by frictional sliding at the wall of the granular flow zone. The central localization of erosion is therefore the result of either a velocity threshold or a threshold in wall-normal stress (therefore frictional shear stress) – or a combination of both – surpassed in the faster, deeper flow zone near the drum axis.

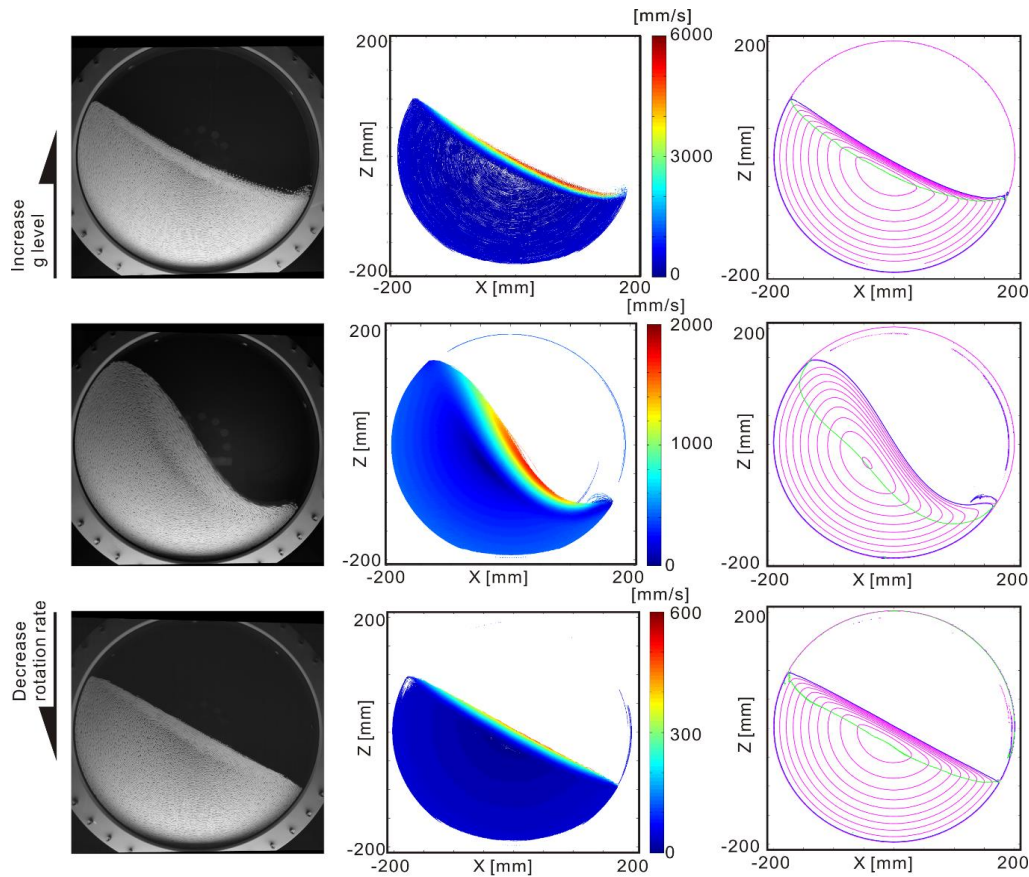


**Fig. 12** Series of experiments at different effective  $g$  and rotation rates. Top row: 20 rpm at 50  $g$ ; middle row: 20 rpm at 1  $g$ ; bottom row: 2 rpm at 1  $g$ . Left column: long exposure images for different flow conditions; middle column: corresponding velocity fields; right column: corresponding stream lines.

## 5. DISCUSSION AND CONCLUSIONS

In this study we have demonstrated the feasibility of using a centrifuge to scale up table-top-size experiments with granular flows to drive erosion of material similar to natural bedrock. We have developed several methods for quantifying the patterns and rates of granular flow and their consequent boundary erosion. We have shown that these methods are accurate and reliable enough to provide the kinds of measurements needed to build an empirical law for sliding wear at the margins of a dry dense granular flow. Furthermore, based on pilot experiments not described here, we anticipate that wet granular flows that better mimic true (i.e., wet and muddy) debris flows will also be amenable to this kind of treatment.

As *Brucks et al.*, [2007] have pointed out, granular flow experiments at effective  $g$  levels over 10  $g$  are prone to non-negligible Coriolis forces. For our experimental setup, the Coriolis force acts normal to the direction of grain flow, i.e., at a small angle to the vertical. As such it will have a second-order effect on

the stress distribution in the flow layer and a modest effect on the rate and pattern of wall erosion. We plan to investigate its effect in more detail through further theoretical development and laboratory experimentation.

The rate of wear induced by a grain sliding over dry rock is a function of the contact force, its contact area, its speed of sliding, and the material properties of the two substrates. Together the contact force and area determine the contact stress and therefore the local damage process. In our simple flow model, we treat stress in a continuum sense only. In forging a sliding erosion law for granular flow, a key challenge is going to lie in linking such continuum stress to contact forces at the walls and across the granular matrix. What is more, it may be that force fluctuations are more important than mean force, as *Hsu*, [2010] has suggested. We are working with a non-smooth contact dynamics model [*Smith et al.*, 2012] of channelized granular to explore such issues.

On the long term, the observation of a velocity-stress threshold in the wear process may be of use in the mapping of debris flow erosion hazard.

**Table 1** Summary of erosion plate experiments in which a disk of synthetic rock is exposed to successive granular flows

States before/after	grain size [mm]	grain shape	run time	rotation rate [rpm]	g-level	weight change [g]
S1 to S2	2.3	spherical	30 min	30	50	Not measured
S2 to S3	2.3	spherical	30 min	30	1	0.076
S3 to S4	2.3	spherical	30 min	30	50	14.835
S4 to S5	4	angular	36 sec	48	50	4.806
S5 to S6	4	angular	5 min	30	50	21.483
S6 to S7	4	spherical	10 min	45	50	26.238
S7 to S8	2.3	spherical	30 min	30	50	10.088

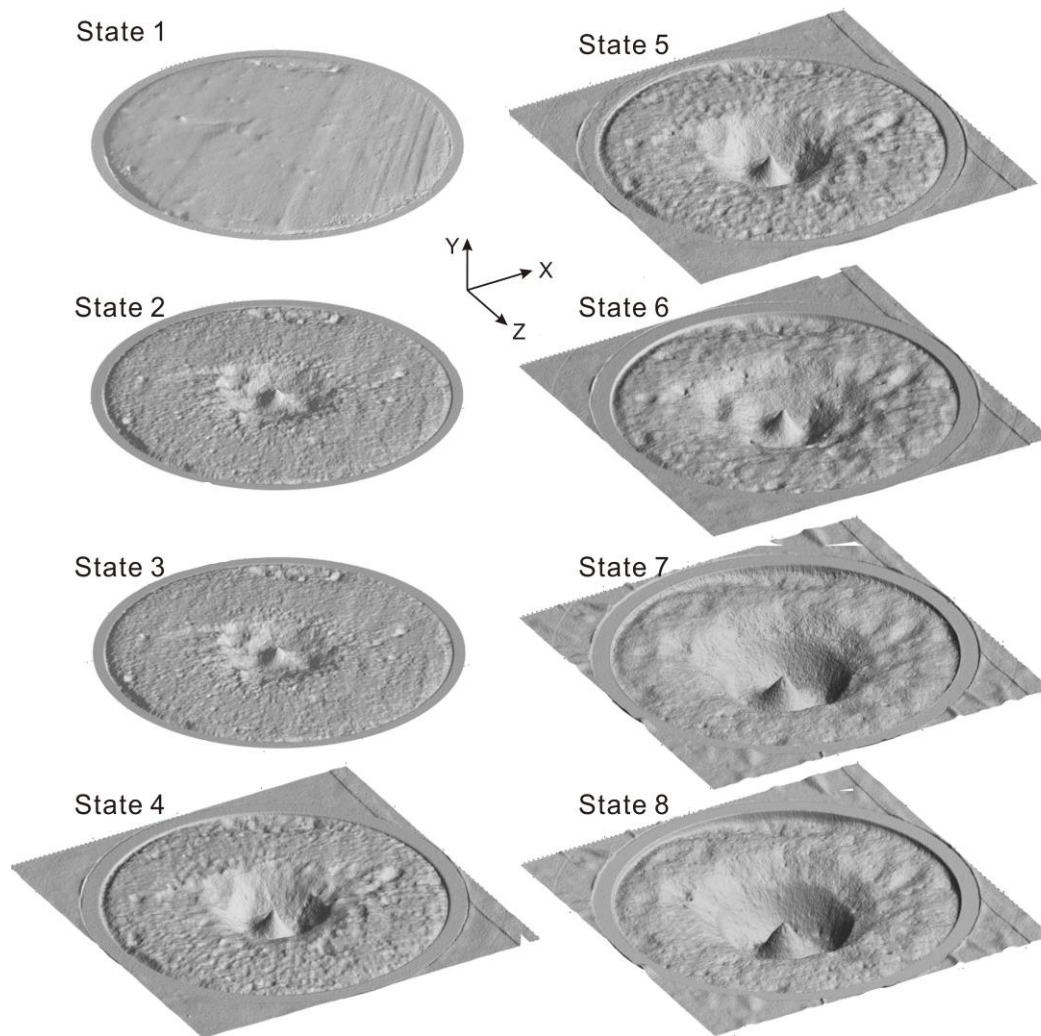


**Fig. 13** Microtopography of the erosion plate for successive states.

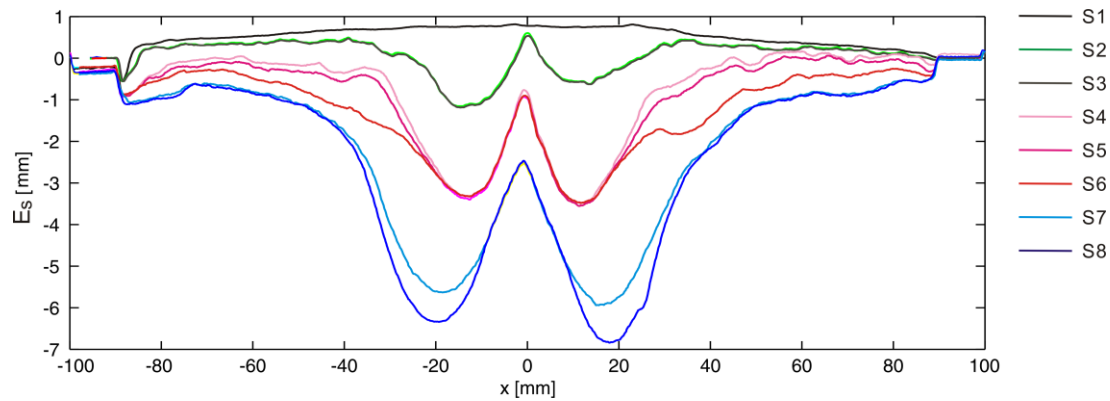


**Fig. 14** Cross-section of the erosion plate at  $z = 0$

## REFERENCES

- Adrian, R.J. (1991): Particle-imaging techniques for experimental fluid mechanics. *Annu. Rev. Fluid Mech.*, Vol. 23, pp. 261–304.
- Ahn, H., Brennen, C.E., and Sabersky, R.H. (1991): Measurements of velocity, velocity fluctuation, density, and stresses in chute flows of granular materials. *Transactions of the ASME*, Vol. 58, pp. 792-803.
- Azanza, E., Chevoir, F., and Moucheron, P. (1999): Experimental study of collisional granular flows down an inclined plane. *Journal of Fluid Mech.*, Vol. 400, pp. 199-227.
- Boateng, A.A., (1998): Boundary layer modeling of granular flow in the transverse plane of a partially filled rotating cylinder. *Int. Journal of Multiphase Flow*, Vol. 24(3), pp. 499-521.
- Berzi, D., and Jenkins, J.T. (2008): A theoretical analysis of free-surface flows of saturated granular-liquid mixtures. *Journal of Fluid Mech.*, Vol. 608, pp. 393-410.
- Brucks, A., Arndt, T., Ottino, J.M., and Lueptow, R.M. (2007): Behavior of flowing granular materials under variable  $g$ . *Physical Review E*, Vol. 75, pp. 032301.
- Buchholtz, V., and Pöschel, T. (1997): Force distribution and comminution in ball mills. In D.E. Wolf, P. Grassberger (eds.), *Friction, Arching, Contact Dynamics*, World Scientific (Singapore, 1997), pp. 265-273.
- Chien, F.-C., and Kuo, H.-C. (2011): On the extreme rainfall of Typhoon Morakot (2009). *Journal of Geophysical Research*, Vol. 116, pp. D05104, doi:10.1029/2010JD015092.
- Capart, H., Young, D.L., and Zech, Y. (2002): Voronoi imaging methods for the measurement of granular flows. *Experiments in Fluids*, Vol. 32, pp. 121–135.
- da Cruz, F., Emam, S., Prochnow, M., Roux, J.N., and Chevoir, F. (2005): Rheophysics of dense granular materials: Discrete simulation of plane shear flows. *Phys. Review E*, Vol. 72, pp. 021309.
- Ding, Y.L., Seville, J.P.K., Forster, R., and Parker, D.J. (2001): Solids motion in rolling mode rotating drums operated at low to medium rotational speeds. *Chemical Engineering Science*, Vol. 56, pp. 1769-1780.
- Fonstad, M. A., Dietrich, J. T., Courville, B. C., Jensen, J. L. and Carbonneau, P. E. (2013): Topographic structure from motion: A new development in photogrammetric measurement. *Earth Surface Processes and Landforms*, Vol. 38, pp. 421–430. doi: 10.1002/esp.3366.
- Forterre, Y. and Pouliquen, O. (2008): Flows of dense granular media. *Annual Review of Fluid Mechanics*, Vol. 40, pp. 1-24.
- GDR Midi (2004): On dense granular flows. *European Physical Journal E*, Vol. 14, pp. 341-365.
- Hsu, L., Dietrich, W.E., and Sklar, L.S. (2008): Experimental study of bedrock erosion by granular flows. *Jour. Geophysical Research*, Vol. 113, pp. F02001 doi:10.1029/2007JF000778.
- Hsu, L. (2010): Bedrock erosion by granular flow. Ph.D. thesis, University of California, Berkeley.
- Iverson, R.M. (1997): The physics of debris flows. *Reviews of Geophysics*, Vol. 35(3), pp. 245-296.
- Jop, P., Forterre, Y., and Pouliquen, O. (2005): Crucial role of sidewalls in dense granular flows: Consequences for the rheology. *Journal of Fluid Mech.*, Vol. 541, pp. 167-192.
- Major, J. J. (1997): Depositional processes in large-scale debris-flow experiments. *Journal of Geology*, Vol. 105, pp. 345-366, doi:10.1086/515930.
- Ni, W. J. (2005): Groundwater drainage and recharge by geomorphically active gullies. MSc thesis, Department of Civil Engineering, National Taiwan University.
- Parsons, J.D., Whipple, K.X., and Simoni, A. (2001): Experimental study of the grain-flow, fluid-mud transition in debris flows. *Journal of Geology*, Vol. 109, pp. 427-447.
- Ristow, G.H. (1996): Dynamics of granular materials in a rotating drum. *Europhysics Letters*, Vol. 34(4), pp. 263-268.
- Savage, S.B. (1984): The mechanics of rapid granular flows. *Advances in Applied Mechanics*, Vol. 24, pp. 290-365.
- Smith, B., Kaufman, D.M., Vouga, E., Tamstorf, R., and Grinspun, E. (2012): Reflections on simultaneous impact. *ACM Transactions on Graphics*, Vol. 31(4), pp. 106:1–106:12.
- Verhoeven, G. (2011): Taking computer vision aloft-archaeological three-dimensional reconstructions from aerial photographs with Photoscan. *Archaeol. Prospect.*, Vol. 18, pp. 67–73. doi: 10.1002/arp.399.
- Xie, B. and Zhang, F. (2012): Impacts of typhoon track and island topography on the heavy rainfalls in Taiwan associated with Morakot (2009). *Monthly Weather Review*, Vol. 140, pp. 3379–3394. doi: 10.1175/MWR-D-11-00240.